AL Saadi, F. S., Champneys, A. R., & Jeffrey, M. R. (2024). Wave-pinned patterns for cell polarity — a catastrophe theory explanation. *SIAM Journal on Applied Dynamical Systems*, *23*(1), 721-747. https://doi.org/10.1137/22M1509758

Wave-pinned patterns for cell polarity — a catastrophe theory explanation *

Fahad Al Saadi† Alan R. Champneys‡ Mike R. Jeffrey†

September 22, 2023

Abstract

A class of four-component reaction-diffusion systems are studied in one spatial dimension, with one of four specific reaction kinetics. Models of this type seek to capture the interaction between active and inactive forms of two G-proteins, known as ROPs in plants, thought to underly cellular polarity formation. The systems conserve total concentration of each ROP, which enables reduction to simple canonical forms when one seeks conditions for homogeneous equilibria or heteroclinic connections between them. Transitions between different multiplicities of such states are classified using a novel application of catastrophe theory. For the time-dependent problem, the heteroclinic connections represent so-called wave-pinned states that separate regions of the domain with different ROP concentrations. It is shown numerically how the form of wave-pinning reached can be predicted as a function of the domain size and initial total ROP concentrations. This leads to state diagrams of different polarity forms as a function of total concentrations and system parameters.

pattern formation, heteroclinic orbits, catastrophe theory, wave pinning, cell polarity.

35K57, 92C15, 34C37

1 Introduction

Polarity formation is a fundamental and essential aspect of the development of just about every eukaryotic cell. This is the process by which a cell gains its initial asymmetry in order to develop its specific structure [28]. This, in turn, enables patterning and differentiation at the level of tissue and organ [37]. Cell polarisation mechanisms are regulated by signalling GTPases, which are

*submitted 15th July 2022 The work of FAlS was supported by the Ministry of Higher Education, Research and Innovation Oman and the Military Technological College, Oman.

†Department of Systems Engineering, Military Technological College, Muscat, Oman; and Department of Engineering Mathematics, University of Bristol (fa17741@bristol.ac.uk)

‡Department of Engineering Mathematics, University of Bristol, Bristol BS8 1TR (a.r.champneys@bristol.ac.uk, mike.jeffrey@bristol.ac.uk

a form of small G-proteins, often called rho-proteins. These proteins freely diffuse both in inactive form within the cell body and in active forms, which are bound to the cell membrane. The process of activation is thought to be autocatalytic mediated guanine exchange factors (GEFs), whereas de-activation is more passive, occurring through (the confusingly named) GTPase-activating proteins, or GAPs [4, 27].

Pioneering work by Mori *et al.* [25] distills a simple mathematical model of the dynamics of G-proteins in a 1D domain (which we can think of as representing the longitudinal co-ordinate of a long cell that captures the essence of the biology of more complex reaction-kinetic models. The model in [25] takes the form of a pair of reaction-diffusion equations for concentrations $u(x,t)$ and $v(x,t)$ for active and inactive forms of a single G-protein species:

$$\frac{\partial u}{\partial t} = \delta^2 \frac{\partial^2 u}{\partial x^2} - \eta u + v + \gamma \frac{u^2 v}{1+u^2}, \tag{1.1a}$$

$$\frac{\partial v}{\partial t} = \frac{\partial^2 v}{\partial x^2} + \eta u - v - \gamma \frac{u^2 v}{1+u^2}, \tag{1.1b}$$

Here the diffusion ratio $\delta \ll 1$, reflects the property that the inactive form is free to diffuse in the cytosol whereas the active form is membrane-bound and therefore diffuses more slowly. The positive dimensionless parameters γ and η represent relative importance of the passive and autocatalytic elements of the GEF-mediated activation of G-protein compared with their GAP-mediated deactivation.

Note that the diffusion-free kinetics of (1.1a) and (1.1b) are equal and opposite. As a consequence of this, natural zero-flux (Neumann) boundary conditions ensure that the total concentration

$$C_T = \int_{\mathcal{D}} (u+v) dx$$

of the G-protein is conserved, and is only a function of the initial conditions. It also means that there is a single nullcline in phase space and there are a continuum of different possible homogeneous equilibria.

The results in [25, 26] highlight a phenomenon for models of the form (1.1) that the authors call *wave pinning*; see [15] for a review. This occurs if parameters and initial total concentration are set within the region of bistability between high and low active species concentrations, then a robust back-and-front polarisation will emerge as the unique (up to reflection symmetry) attracting steady state. Such states represent spatial heteroclinic orbits between the bistable homogeneous equilibria, which are saddle points in the phase space of the so called *spatial dynamics problem* where x is treated as a time-like variable. When posed on a finite domain with Neumann boundary conditions, the precise parameter value at which the spontaneous symmetry-breaking occurs, and the position of the sharp transition point within the domain is determined by the total concentration C_T. This process has been shown to be robust, to a certain extent for models of the form eq:Mori [16, 26, 39, 40], provided an equivalent of C_T is conserved.

One drawback of the simple model (1.1) is that it models a single G-protein. Yet, in animals and uni-cellular organisms, the mechanism typically involves the cross-talk between three (or more) mutually inhibitive G-protein species known as *rho*, *rac* and *cdc42*. [16, 31, 43, 44]. The homologue in plants are called *ROP*, which literally stands for *rho of plants*; and since cells cannot travel through tissue, ROP-based polarity mechanisms are crucial to tissue organisation, both through directing growth [12,42] and through control of the hormone, auxin [13, 21,22,32]. Canonical plant polarity processes that are widely studied include the positioning of the growth of hair-like protuberances in the root trophoblast [5,6, 33,38] and the jigsaw-piece shapes formed by leaf pavement cells [10,34]. While polarity mechanisms in plants can occur without cross-talk, for the pavement cells it is thought that at least two families of G-protein are required; ROP2 and ROP6, with the former localising at lobes and the latter at indentations.

Several authors have proposed extensions to models of the form eq:Mori to consider the cross-talk between two or more G-proteins; see e.g. [1, 16, 18, 45]. The purpose of the present paper is to extend the notion of spontaneous polarity formation through wave pinning in such models. Simulation results have shown these models to feature a richer array of polarised patterns, and our aim is to provide some mathematical explanation to what has been observed in models for the interaction of two G-proteins which leads to a system of four reaction-diffusion equations; see sec:models below for the form of these equations.

Our approach will be to extend the methodology developed in [26,39] to deal with the higher-dimensionality of the state space. This involves, first, the use of spatial dynamics to determine parameter regions in which there is bistability between equilibria and where heteroclinic orbits exist. We shall find that the phase space can be reduced because of two invariants, which parameterise different families of equilibria and heteroclinic orbits between them, and we characterise these families using catastrophe theory. Second, we turn to the full PDE dynamics on a long finite domain, and show how two consideration of two conserved quantities analogous to C_T leads to a characterisation of the different types of wave-pinning seen for different overall concentrations of the two G-proteins.

To characterize the equilibria of the PDE we adapt the concept of *elementary catastrophes* for use with vector fields. While dynamical systems theory provides a classification of bifurcations of equilibria of vector fields, see e.g. [3], it does not provide explicit methods with which to find such events in general (i.e. for general numbers of variables and parameters). Instead, we describe here how to use Thom's simpler notion of elementary catastrophes [30, 36] to find such bifurcation points, and use it to develop a general method that has been outlined more completely in [20]. In the present problem we use this to show that a butterfly catastrophe creates up to 5 equilibria. Catastrophes up to codimension 6, a star catastrophe, can be found in the system, but as we show, the star occurs at biologically irrelevant parameters.

The rest of the paper is outlined as follows. sec:models sets out the general four-dimensional system of reaction-diffusion equations to be studied, including different possible forms for the kinetic terms. stedstat contains the main

results of the paper by studying steady-state solutions of the models in question. After rescaling of variables, the steady-state problem can be posed as a reversible dynamical system in an appropriate phase space, which preserves two first integrals. Bifurcation diagrams of different spatially homogeneous states as values of these integrals change can be established analytically, and families of heteroclinic equilibria between these states can be computed numerically. It is then shown how the bifurcation diagrams can be understood using catastrophe theory, and we describe how this idea can be applied to vector fields in general. trnhete then shows how the defining equations derived from the catastrophe theory can explain how the computed bifurcation diagrams transform as system parameters are varied. This leads to the eventual destruction of all nontrivial steady states upon increasing the diffusion ratio δ. overalldynamic then considers solutions to the initial-value problem using numerical methods, and shows how different kinds of wave-pinned solutions arise for different values of the total concentrations of each ROP species. All the computations in stedstat–5 are performed for one particular form of kinetic terms, although the methodology is general. othemodel then briefly presents equivalent results for three different kinetic forms considered in the literature. Finally, conhete draws conclusions and suggests avenues for future work.

2 Cell polarity models

We start by describing the general form of a simple model of intracellular patterning [1, 16] based on the diffusion of two types of interacting molecular components (A and B). In reality, each component may represent classes of several types of ROP, but for simplicity, each component is treated as a single entity. The two components can each occur in two forms: active and membrane-bound, denoted by using an asterisk; and inactive and unbound, denoted without asterisk. The inactive components are assumed to have a higher diffusion constant as they are free to move within the cytosol. The kinetics of activation and deactivation of each component is supposed to be similar to that of (1.1), with the addition of cross inhibition; specifically that A^* reinforces deactivation of B^*, and vice versa. The reaction-diffusion dynamics of such a system can thus be expressed by the following system of partial differential equations (PDEs):

$$\frac{\partial A^*}{\partial t} = D_{A^*}\frac{\partial^2 A^*}{\partial x^2} + F(A^*, A, B^*, B), \tag{2.2a}$$

$$\frac{\partial A}{\partial t} = D_A\frac{\partial^2 A}{\partial x^2} - F(A^*, A, B^*, B), \tag{2.2b}$$

$$\frac{\partial B^*}{\partial t} = D_{B^*}\frac{\partial^2 B^*}{\partial x^2} + G(A^*, A, B^*, B), \tag{2.2c}$$

$$\frac{\partial B}{\partial t} = D_B\frac{\partial^2 B}{\partial x^2} - G(A^*, A, B^*, B), \tag{2.2d}$$

where functions F and G describe the activation and inhibition dynamics of two ROP species A and B. See equations (2.5)–(2.8) below for different possible

forms of F and G. Owing to the assumptions about diffusion described above, in what follows we suppose $D_{A^*}, D_{B^*} \ll D_A, D_B$, and more specifically that

$$D_{A^*} = D_{B^*} = \delta \ll 1 \qquad \text{and} \quad D_A = D_B = 1.$$

Since the active and inactive components cannot leave or enter the cell, we enforce the Neumann boundary conditions on a finite domain $x \in (-\ell, \ell)$:

$$\mathbf{U}_x(\pm\ell) = 0, \qquad \text{where} \quad \mathbf{U} = (A, A^*, B, B^*).$$

The model presumes that for each ROP species there is inter-conversion between active and inactive forms, yet each ROP is neither created nor destroyed. Therefore, we find two conservation laws. Specifically, adding (2.2a) and (2.2b) and integrating over the domain we have

$$\int_{-l}^{l} \frac{\mathrm{d}}{\mathrm{d}t} \hat{A} dx = \int_{-l}^{l} \left[D_{A^*} A^*_{xx} + D_A A_{xx} \right] dx, \tag{2.3}$$

where $\hat{A} = A^* + A$. Under Neumann boundary conditions at $x = \pm l$, the integral on the right-hand side of (2.3) vanishes. Thus, we have

$$\frac{\mathrm{d}}{\mathrm{d}t} \int \hat{A} = 0 \qquad \text{or equivalently} \qquad \int \hat{A} = \text{constant} := A_T \ , \tag{2.4}$$

and similarly for B.

Based on different choices for F and G, one can obtain different GTPase models that illustrate the intracellular partitioning dynamics. Several such models have been described in the literature, which we delineate as follows.

Model I: intracellular partitioning model for tissue cell polarity in plants and animals presented by Abley *et al* [1]:

$$F = (\eta\, A^* + \rho)\, A - (\alpha\, B^* + \mu)\, A^* \tag{2.5a}$$

$$G = (\eta\, B^* + \rho)\, B - (\alpha\, A^* + \mu)\, B^*. \tag{2.5b}$$

Here α is the cross-inhibition rate between the membrane-bound polarity component, η is the auto-activation rate, μ is the membrane unbinding rate, and ρ describes the membrane binding rate.

Model II: a modification of the model in [1], proposed in [2]:

$$F = \left(\eta\, {A^*}^2 + \rho\right) A - (\alpha\, B^* + \mu)\, A^* \tag{2.6a}$$

$$G = \left(\eta\, {B^*}^2 + \rho\right) B - (\alpha\, A^* + \mu)\, B^*, \tag{2.6b}$$

where the parameters α, η, μ and ρ have the same meaning as in (2.5).

Model III: intracellular partitioning model for "juicy fruit" by Grieneisen *et al.* [16]:

$$F = \left(\beta + \eta\,\alpha\,\mu^2 A^{*2}\left(\mu^2 + A^{*2} + B^{*2} + \frac{\alpha}{c_a}\right)^{-1}\right) A - \rho\, A^*, \tag{2.7a}$$

$$G = \left(\beta + \eta\,\alpha\,\mu^2 B^{*2}\left(\mu^2 + A^{*2} + B^{*2} + \frac{\alpha}{c_a}\right)^{-1}\right) B - \rho\, B^*. \tag{2.7b}$$

Here α denotes homogeneous auxin level, β captures the rate of auxin-independent basal activation rate, η gives the auto-activation strength, μ is the saturation constant in ROP auto-activation and cross-inhibition, c_a is a saturation constant in activation by auxin, and ρ defines the deactivation rate .

Model IV: a mutual inhibition model introduced by Holmes *et al.* [18]:

$$F = \left(b + \frac{\alpha}{1 + B^{*n}}\right) A - dA^*, \tag{2.8a}$$

$$G = \left(b + \frac{\alpha}{1 + A^{*n}}\right) B - dB^*. \tag{2.8b}$$

Here the parameters α and b represent the strength of feedback and basal activation, respectively, and d is the rate of GTPase inactivation.

Verschueren *et al* [39, 40] applied the Maxwell equal energy principle to the time-independent version of the simple wave-pinning model (1.1) to produce a condition for front selection. Their method reduces the coupled system to a single second-order ordinary differential equation (ODE) which can be analysed in a phase plane. We shall now attempt to apply the same theory to the two-species model (2.2). Consequently, we look for steady-state solutions by introducing new variables as follows:

$$S(x) = \delta A^*(x) + A, \quad u(x) = \delta A^*(x) - A, \tag{2.9a}$$

$$E(x) = \delta B^*(x) + B, \quad v(x) = \delta B^*(x) - B. \tag{2.9b}$$

Then substituting (2.9) into the time-independent version of (2.2), we obtain the following system of second-order ODEs in space:

$$\frac{\partial^2 S}{\partial x^2} = 0, \tag{2.10a}$$

$$\frac{\partial^2 u}{\partial x^2} = -2F(u, S, v, E), \tag{2.10b}$$

$$\frac{\partial^2 E}{\partial x^2} = 0, \tag{2.10c}$$

$$\frac{\partial^2 v}{\partial x^2} = -2G(u, S, v, E). \tag{2.10d}$$

Due to the boundary conditions, the only allowable solutions to (2.10a) and (2.10c) are constant. Thus S and E effectively become independent parameters and (2.10) is reduced to two second-order equations in variables $u(x)$ and $v(x)$.

In general we will consider each of the specific forms of the function F and G given by equations (2.5)-(2.8). However, for the development of the theory in paper we exclusively study model II as our worked example. Related results for the other models are treated briefly in othemodel.

3 Steady states and their heteroclinic connection

To characterise the wave-pinned solutions of (2.2) and (2.6), it is useful to pose the spatial system (2.10) on an infinite domain, and look for heteroclinic connections between the homogeneous steady states. We find that up to nine steady states can exist in the model, and we shall first find regions of parameter space where they exist, and study their stability, before determining which may be connected by heteroclinic orbits. The outcome is summarized in the example bifurcation diagram in Hetesolution, showing bifurcation sets of steady states (black curves), and existence sets of heteroclinic orbits (coloured curves, with examples of heteroclinic illustrated in the graphs (a)-(e)). We also show how to formalise the conditions for different kinds of equilibria to exist using catastrophe theory.

To find the steady states, let us first re-write the model more conveniently. For the kinetics abley2, the time-independent model spatialsys can be written in the form

$$\begin{aligned} u'' &= -2F = 2\rho(u-S) + \left(\frac{2\mu}{\delta} + \frac{\eta}{2\delta^2}(u^2-S^2) + \frac{\alpha}{\delta^2}(v+E)\right)(u+S)\,, \\ v'' &= -2G = 2\rho(v-E) + \left(\frac{2\mu}{\delta} + \frac{\eta}{2\delta^2}(v^2-E^2) + \frac{\alpha}{\delta^2}(u+S)\right)(v+E)\,. \end{aligned} \tag{3.11}$$

Note that (3.11) has six independent parameters $S, E, \frac{\mu}{\delta}, \frac{\eta}{2\delta^2}, \frac{\alpha}{\delta^2}, \rho$. Letting $u = x - \frac{1}{3}S$ and $v = y - \frac{1}{3}E$ eliminates the u^2 and v^2 terms to give the simpler expressions

$$\begin{aligned} x'' &= \frac{\eta}{2\delta^2}\hat{f}\,, \qquad \hat{f} = x^3 + kxy + ax + ry + b\,, \\ y'' &= \frac{\eta}{2\delta^2}\hat{g}\,, \qquad \hat{g} = y^3 + kxy + cy + sx + d\,, \end{aligned} \tag{3.12}$$

effectively scaling the parameter $\frac{\eta}{2\delta^2}$ out of the following analysis, and giving us

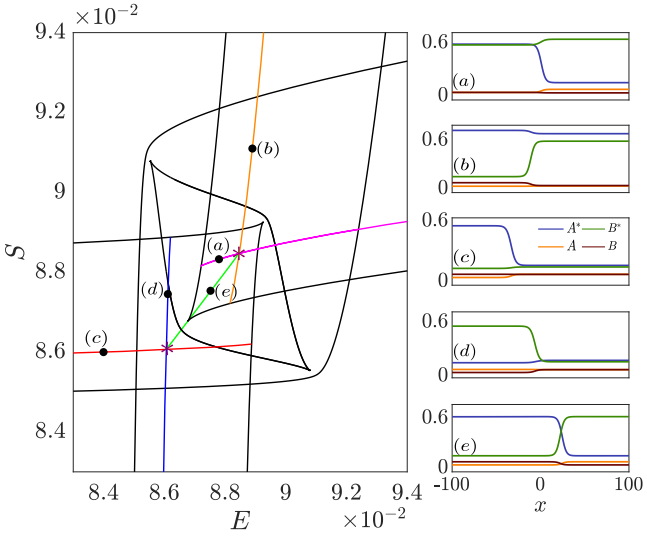

Figure 1: Bifurcation diagram in E and S of the reduced system (2.10) for (2.6). System parameter values used are $\eta = 2$, $\mu = 0.05$, $\rho = 0.06$, $\alpha = 0.005$ and $\delta = 0.08$. Here black lines represent curves of fold bifurcations and coloured lines show curves on which different kinds of heteroclinic connection exist. A full explanation of this bifurcation diagram is the main purpose of stedstat.

a new set of parameters

$$
\begin{aligned}
k &= \frac{2\alpha}{\eta}\,, \qquad r = \frac{4\alpha S}{3\eta}\,, \qquad s = \frac{4\alpha E}{3\eta}\,,\\
a &= \frac{4}{\eta}\left\{\frac{\alpha E - \eta S^2}{3} + \delta(\mu + \delta\rho)\right\}\,,\\
c &= \frac{4}{\eta}\left\{\frac{\alpha S - \eta E^2}{3} + \delta(\mu + \delta\rho)\right\}\,,\\
b &= \frac{8S}{3\eta}\left\{\frac{1}{3}(\alpha E - \frac{2}{3}\eta S^2) + \delta(\mu - 2\rho\delta)\right\}\,,\\
d &= \frac{8E}{3\eta}\left\{\frac{1}{3}(\alpha S - \frac{2}{3}\eta E^2) + \delta(\mu - 2\rho\delta)\right\}\,.
\end{aligned}
\tag{3.13}
$$

Note that k, r, s, a, b, c, d, constitute only 5 independent parameters, because they satisfy

$$
\begin{aligned}
a - c &= s - r + \frac{3\eta^2}{4\alpha^2}(s^2 - r^2)\,,\\
\frac{b}{r} - \frac{d}{s} &= \frac{\eta}{2\alpha}(s - r) + \frac{\eta^3}{4\alpha^3}(s^2 - r^2)\,.
\end{aligned}
$$

The system is invariant under the change $(x, y, r, s) \to (y, x, s, r)$ (or $(u, v, E, S) \to (v, u, S, E)$ in the original coordinates). To exploit this let us change coordinates

one more time to

$$X = x + y \,, \qquad Y = x - y \,. \tag{3.14}$$

Then the second-order system redueAbly becomes $(X'', Y'') = \frac{\eta}{2\delta^2}(\hat{F}, \hat{G})$, where

$$\begin{aligned}
\hat{F} &= \frac{1}{4}X(X^2 + 3Y^2) + \frac{1}{2}k(X^2 - Y^2) + \frac{1}{2}(a + c + r + s)X \\
&\quad + \frac{1}{2}(a - c - r + s)Y + b + d \,, \\
\hat{G} &= \frac{1}{4}Y(3X^2 + Y^2) + \frac{1}{2}(a - c + r - s)X + \frac{1}{2}(a + c - r - s)Y \\
&\quad + b - d \,.
\end{aligned} \tag{3.15}$$

Finally, we can write this as a first order 4-dimensional system by letting $(X', Y') = \frac{\eta}{2\delta^2}(Z, W)$, giving

$$(X', Z', Y', W') = \Big(\frac{\eta}{2\delta^2}Z,\ \hat{F},\ \frac{\eta}{2\delta^2}W,\ \hat{G}\Big) \,. \tag{3.16}$$

We will show in the following two subsections that this four-dimensional system has up to nine equilibria, and we identify these with the following labels. There are three equilibria that we label

$$(X_I, Y_I) \,, \quad (X_{II}, Y_{II}) \,, \quad (X_{III}, Y_{III}) \,, \tag{3.17}$$

such that $X_I \le X_{II} \le X_{III}$,, and when $S = E$ these lie on $Y = 0$ where $\hat{G} = 0$. The remaining six equilibria form three pairs of points that we label as

$$(X_1^{\pm}, Y_1^{\pm}) \,, \quad (X_2^{\pm}, Y_2^{\pm}) \,, \quad (X_3^{\pm}, Y_3^{\pm}) \,, \tag{3.18}$$

such that $X_1 \le X_2 \le X_3$, and $Y_i^- \le 0 \le Y_i^+$, and when $S = E$ we will show that these lie on an ellipse defined by the condition $\hat{G} = 0 \ne Y$.

Examples of these equilibria are illustrated in spatiEgen for the case $E = S$. For $S \ne E$ we label the equilibria by continuation from $S = E$, and an example is shown in spatiEgen2. The equilibria are shown as lying at the intersection of the nullclines $\hat{F} = 0$ (red curves) and $\hat{G} = 0$ (purple curves). Shown inset in these figures is the stability of the equilibria, within this ODE system, which we derive in sec:eigenvalues below. The nature of these equilibria will enable us to infer the existence of heteroclinic orbits. When $S = E$ the system is symmetric about $Y = 0$, and a heteroclinic solution (cyan curve) can then exist connecting the '1+' and '1−' equilibria, as shown in spatiEgen. The symmetry is broken when $S \ne E$, and a heteroclinic connection (cyan curve) can then exist connecting the '1+' and 'I' equilibria, as shown in spatiEgen2. Note the heteroclinic solution does not pass through the '2+' equilibrium in the full four-dimensional space of (X, X', Y, Y').

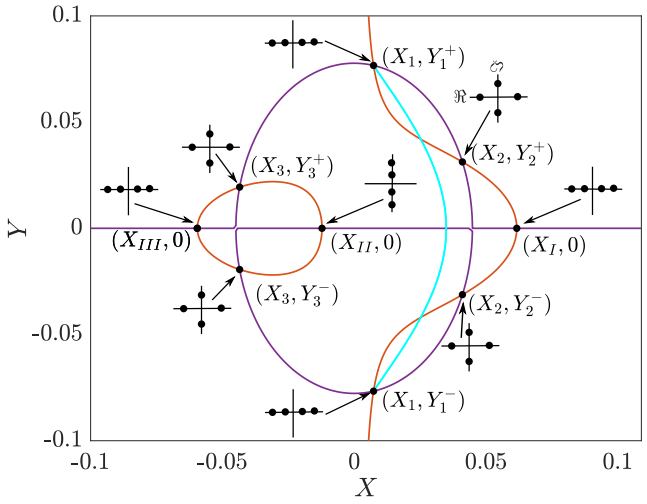

Figure 2: Nine equilibria lie at the intersections of the nullclines $\hat{F} = 0$ (red) and $\hat{G} = 0$ (purple). The heteroclinic solution (cyan) connects the '1+' and '1−' equilibria. Insets show the (spatial) eigenvalues of each equilibrium, in the complex plane with location of eigenvalues denoted by bold dots. Parameters chosen are $\eta = 2$, $\mu = 0.05$, $\rho = 0.06$, $\alpha = 0.005$ and $\delta = 0.08$, and $S = E = 0.0878$.

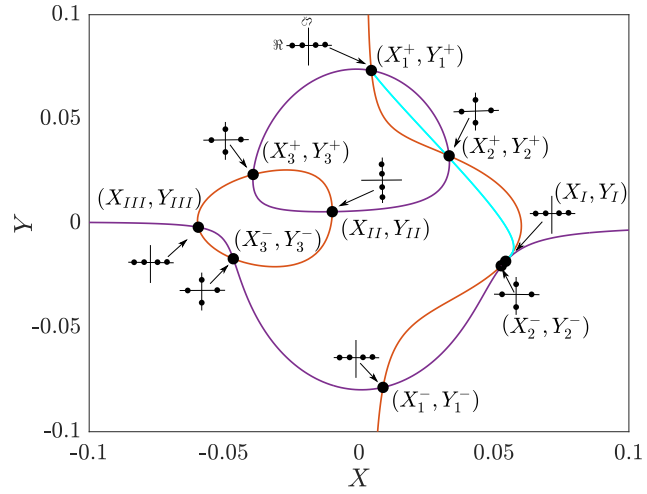

Figure 3: A perturbation of spatiEgen for $\eta = 2$, $\mu = 0.05$, $\rho = 0.06$, $\alpha = 0.005$ and $\delta = 0.08$, $E = 0.0881606$ and $S = 0.0872160$. The heteroclinic solutions now connects the '1+' and 'I' equilibria. Other curves are as in spatiEgen.

3.1 Locating the equilibria

When $S = E$ the model simplifies such that its 9 equilibria can be found explicitly. Taking trans with $S = E$ gives $r = s$, $a = c$, $b = d$, and substituting these into XYgen1 gives

$$\begin{aligned}\hat{F} &= \frac{1}{4}X(X^2 + 3Y^2) + \frac{1}{2}k(X^2 - Y^2) + (a + r)X + 2b \,, \\ \hat{G} &= Y\left\{\frac{1}{4}(3X^2 + Y^2) + (a - r)\right\} \,. \end{aligned} \tag{3.19}$$

Like the general system this has up to 9 equilibria, but here they can be decoupled into two groups of equilibria where $\hat{G} = 0$, namely 3 equilibria on the surface $Y = 0$ labelled by XIII1, and six equilibria on the surface $\frac{1}{4}(3X^2 + Y^2) + (a - r) = 0$ labelled by X121, as we will now define.

On $Y = 0$ the system XY2 is given by

$$\begin{aligned} X' &= \frac{\eta}{2\delta^2}Z \,, \qquad Y'' = Y' = 0 \,, \\ Z' &= \frac{1}{4}X^3 + \frac{1}{2}kX^2 + (a + r)X + 2b \,. \end{aligned} \tag{3.20}$$

(This means the system is invariant on $Y = 0$, but this property will not be of further use here). The zeroes of this subsystem give us the 3 equilibria which we denote by XIII1, where X_I, X_{II}, X_{III}, are the real roots of

$$\frac{1}{4}X_i^3 + \frac{1}{2}kX_i^2 + (a + r)X_i + 2b = 0 \,, \qquad i = I, II, III \,. \tag{3.21}$$

For $S \neq E$ these equilibria no longer necessarily lie on $Y = 0$, but we use this same labeling by continuation away from $S = E$.

The elliptical surface $3X^2 + Y^2 = 4(r - a)$ gives a second (albeit not invariant) subsystem of XY2, where it becomes

$$\begin{aligned} X' &= \frac{\eta}{2\delta^2}Z \,, \quad Z' = 0 \,, \quad 3X^2 + Y^2 = 4(r - a) \,, \\ \frac{1}{2}Z' &= -X^3 + k(X^2 + (a - r)) + (2r - a)X + b \,. \end{aligned} \tag{3.22}$$

The zeroes of this provide the six equilibria which we denote by X121. They satisfy $X_i^+ = X_i^- := X_i$, where X_i are the roots of

$$-X_i^3 + k(X_i^2 + (a - r)) + (2r - a)X_i + b = 0 \,, \qquad i = 1, 2, 3 \,. \tag{3.23}$$

and $Y_i^\pm = \pm\{4(r - a) - 3X_i^2\}$. Again, when $S \neq E$ we use this same labeling for the equilibria by continuation away from $S = E$.

These equilibria are shown in spatiEgen for $S = E$. We see the three equilibria (X_1, Y_1), (X_2, Y_2), (X_2, Y_2), lying on the line $Y = 0$, while the six equilibria $(X_I^\pm, Y_I^\pm)$, $(X_{II}^\pm, Y_{II}^\pm)$, $(X_{III}^\pm, Y_{III}^\pm)$, lie on the ellipse $3X^2 + Y^2 = 4(r - a)$, as described by the subsystems in invsys1 and ellipsys1, respectively.

These equilibria are shown in spatiEgen for $S = E$. We see the three equilibria (X_1, Y_1), (X_2, Y_2), (X_2, Y_2), lying on the line $Y = 0$, while the six equilibria $(X_I^{\pm}, Y_I^{\pm})$, $(X_{II}^{\pm}, Y_{II}^{\pm})$, $(X_{III}^{\pm}, Y_{III}^{\pm})$, lie on the ellipse $3X^2 + Y^2 = 4(r - a)$, as described by the subsystems in (3.20) and (3.22), respectively. In spatiEgen2 the system no longer decouples exactly into these subsystems, but we see that the equilibria persist.

As the parameters in the model change, these nullclines deform, causing the equilibria to move and annihilate in a variety of bifurcations. Between spatiEgen and spatiEgen2, for example, the two equilibria (X_I, Y_I) and (X_2^-, Y_2^-) have approached each other and are about to annihilate via a fold bifurcation.

We will identify the bifurcations that occur below. First, let us take a look at the stability of the equilibria found above, to identify which can be connected by heteroclinic orbits.

3.2 Local stability

Only some of the nine equilibria can be involved in heteroclinic orbits generically, namely those with at least a two-dimensional stable or unstable manifold. Let us determine which of the equilibria found in sec:eqs this applies to.

The Jacobian of the system (3.19) in (X, X', Y, Y') space is

$$J = \begin{pmatrix} 0 & 1 & 0 & 0 \\ \frac{3X^2}{4} + \frac{3Y^2}{4} + kX + a + r & 0 & \frac{3XY}{2} - kY & 0 \\ 0 & 0 & 0 & 1 \\ \frac{3XY}{2} & 0 & \frac{3X^2}{4} + \frac{3Y^2}{4} + a - r & 0 \end{pmatrix}. \tag{3.24}$$

For the invariant subsystem on $Y = 0$ given by (3.20) this simplifies to

$$J = \begin{pmatrix} 0 & 1 & 0 & 0 \\ \frac{3X^2}{4} + kX + a + r & 0 & 0 & 0 \\ 0 & 0 & 0 & 1 \\ 0 & 0 & \frac{3X^2}{4} + a - r & 0 \end{pmatrix}, \tag{3.25}$$

with eigenvalues

$$\begin{aligned} \lambda_1 = -\lambda_2 &= \frac{1}{2}\sqrt{3\,X^2 + 4\,a - 4\,r} \qquad \text{and} \\ \lambda_3 = -\lambda_4 &= \frac{1}{2}\sqrt{3\,X^2 + 4\,kX + 4\,a + 4\,r}\,. \end{aligned} \tag{3.26}$$

For the invariant subsystem on the ellipse given by (3.22) the Jacobian sim-

plifies to

$$J = \begin{pmatrix} 0 & 1 & 0 & 0 \\ \frac{Y^2}{2} + kX + 2r & 0 & \frac{Y(3X-2k)}{2} & 0 \\ 0 & 0 & 0 & 1 \\ \frac{3XY}{2} & 0 & \frac{Y^2}{2} & 0 \end{pmatrix}, \tag{3.27}$$

with eigenvalues

$$\begin{aligned} \lambda_1 = -\lambda_2 &= \frac{1}{2}\sqrt{M + 2\sqrt{L}} \qquad \text{and} \\ \lambda_3 = -\lambda_4 &= \frac{1}{2}\sqrt{M - 2\sqrt{L}} \end{aligned} \tag{3.28}$$

where $L = \left(9Y^2 + k^2\right)X^2 - 6k\left(Y^2 - \frac{2}{3}r\right)X + 4r^2$ and $M = 3X^2 + 2kX + 3Y^2 + 4a$.

By evaluating each of these eigenvalue expressions at the respective equilibria of the two subsystems, the resulting eigenvalues are shown as insets in spatiEgen and spatiEgen2 for each of the 9 equilibria. These show that the 'II' equilibrium cannot form heteroclinics because it is a center, while '2' and '3' are saddle-centers with only one-dimensional stable and unstable manifolds, so they do not generically form heteroclinic orbits.

So the equilibria 'I', 'III', and '1±', which are each saddle-nodes with two-dimensional stable and unstable manifolds, are the source of heteroclinic connections. In spatiEgen we see a heteroclinic orbit (cyan curve) that connects the '1+' and '1−' equilibria; this corresponds to the heteroclinic orbit that exists on the green curve in the (S, E)-plane shown in Hetesolution. In spatiEgen2 we see a heteroclinic orbit (cyan curve) that connects the '1+' and 'I' equilibria; this corresponds to the heteroclinic orbit that exists on the blue curve in the (S, E)-plane shown in Hetesolution.

It is not easy to directly find expressions for parameter values at which these different heteroclinic connections exist. It is, however, easy to give bounds for their existence by finding the parameters at which these equilibria are destroyed in bifurcations. The next subsection describes how we compute the heteroclinic orbits computationally, then sec:bif describes how we compute their regions of existence from bifurcations of the equilibria.

3.3 Bifurcations

Hetesolution showed a typical bifurcation diagram for the system in the (S, E)-plane. The black curves show the locations of fold bifurcations. (The coloured curves show the existence of heteroclinic orbits to be discussed later). At each point labelled $(a), (b), (c), (d), (e), (f)$, the equilibria and nullclines are shown in (X, Y) space in fig:clinics, similarly to spatiEgen-spatiEgen2.

We will first identify bifurcations in the $S = E$ system. We shall see that the highest order bifurcations occur when $S = E$, and these turn out to be the most

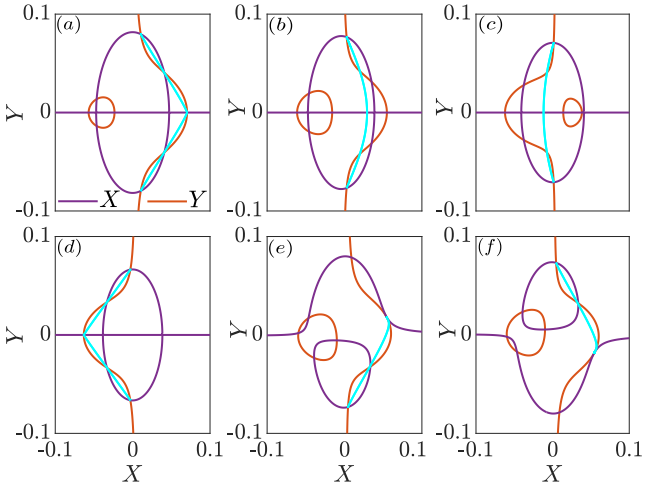

Figure 4: The phase plane for (X,Y) in (3.15) with fixed $\eta = 2$, $\mu = 0.05$, $\rho = 0.06$, $\alpha = 0.005$ and $\delta = 0.08$, showing the nullclines $\hat{F} = 0$ (red) and $\hat{G} = 0$ (purple); the 9 equilibria lie at their intersections. The heteroclinic solution that exists in each case is shown.

significant, as well as having the advantage that we can find them explicitly. We will then give conditions that can be used to find bifurcations more generally when $S \neq E$.

We study the 3 equilibria of the subsystem invsys1 simply by looking at the 3 roots of cubicI. Thus fold bifurcations occur where

$$(27b + 2k^3 - 9k(a + r))^2 = 4(k^2 - 3(a + r))^3 \tag{3.29}$$

and a cusp occurs at

$$b = \frac{1}{27}k^3 \ , \qquad a = \frac{1}{3}k^2 - r \ . \tag{3.30}$$

At these parameters, with $S = E$, the system therefore undergoes fold and cusp bifurcations. For $S \neq E$ the folds continue outward into parameter space to form some of the fold curves as seen in Hetesolution.

The six equilibria of the subsystem in ellipsys1 are studied by considering the 3 roots of cubic1 (with each root corresponding to a pair of equilibria $(X_i^{\pm}, Y_i^{\pm})$). Thus there are 6 equilibria when

$$\begin{aligned} &k^2 > 3a - 6r \qquad \text{and} \\ &4(k^2 + 6r - 3a)^3 > (54b + 2k^3 + 18ak - 9rk)^2 \ , \end{aligned} \tag{3.31}$$

and only 2 equilibria otherwise, with folds occurring at

$$4(k^2 + 6r - 3a)^3 = (27b + 2k^3 + 18ak - 9rk)^2 \tag{3.32}$$

and a cusp occurring at

$$b = -\frac{8}{27}k^3 - rk \ , \qquad a = \frac{1}{3}k^2 + 2r \ . \tag{3.33}$$

At these parameters, with $S = E$, the system therefore undergoes simultaneous fold and cusp bifurcations at symmetric values (given by the '$\pm$' labels) of Y. Again, for $S \neq E$ the folds continue outward into parameter space to form some of the fold curves as seen in Hetesolution.

The two families of bifurcations found above occur *within* each of the two subsets of equilibria identified in sec:eqs. There is one further family of bifurcations that occurs *between* the two subsets, at the point $(X, Y) = (\pm 2\sqrt{(r-a)/3}, 0)$ shared by both of the subsystems $Y = 0$ and $3X^2 + Y^2 = 4(r - a)$. These turn out to be of the greatest interest as they terminate the lines of heteroclinic solutions at the points (e) and (f) in Hetesolution.

To find these bifurcations we need only look for mutual solutions of both cubic equations cubicI and cubic1, therefore lying at $X^2 = \frac{4}{3}(r - a)$ and $Y = 0$. One equilibrium from the subsystem invsys1 and two from the subsystem ellipsys1 coincide when

$$b = \frac{1}{3}\left(k(a - r) \mp \frac{2}{\sqrt{3}}(2r + a)\sqrt{r - a}\right)$$

This therefore defines a cusp bifurcation. Three such cusp points can be seen in Fig. 1.

It can also happen that four equilibria from the ellipse subsystem collide with one from the $Y = 0$ subsystem. This is found by solving for a fold point of cubic1 coinciding with an equilibrium of cubicI, resulting in

$$\begin{aligned} a &= \frac{2}{27}\left(9r - 4k^2 \pm 2k\sqrt{4k^2 + 9r}\right) \ , \\ b &= \frac{1}{27}\left(k(9r - 18a - 2k^2 \mp 2(k^2 + 6r - 3a)^{3/2})\right) \ . \end{aligned} \tag{3.34}$$

This higher-codimension bifurcation is an example of a butterfly catastrophe (see CataTheo, below). For example, if we take $\eta = 2$, $\mu = 0.05$, $\rho = 0.06$, $\alpha = 0.005$, we find numerically that two such degenerate bifurcations occur; at $S = E \approx 0.0972536$, $\delta \approx 0.110666$ and at $S = E \approx 0.0983051$, $\delta = 0.112176$. These two points are, respectively, on the black and grey curves in the (η, δ)-plane represented in butterfly below.

In principle other bifurcations are also possible, but they do not play a role here. For example, folds or cusps can occur within the subsystem $Y = 0$ alone. A higher-order bifurcation can also occur in which all six of the equilibria of the ellipse subsystem annihilate, along with an equilibrium of the $Y = 0$ subsystem, constituting a so-called star singularity (with codimension 6), but this is found to occur only for $r < 0$ and therefore it is not physically relevant here.

All of the analysis above applies only for the simplified case with $S = E$, for which $r = s$, $a = c$, and $b = d$. We have also referred to the bifurcations

found as 'folds', 'cusps', and 'butterflies', without showing that they satisfy the necessary genericity conditions for such a classification from the perspective of singularity theory. To do this, and to extend this analysis to $S \neq E$, requires an understanding of the catastrophe theory.

3.4 Catastrophe theory for vector fields

For the special case of parameters $S = E$ we were able to simplify the system above to show that it undergoes fold, cusp, and butterfly bifurcations. For more general parameters, and to find any other bifurcations (the system can also undergo swallowtails, wigwams, and stars), we require a more general approach amenable to numerical continuation.

Unfortunately, for an ODE system with dimension $n > 1$, there do not appear to exist general criteria in the literature to identify bifurcations beyond codimension one or two (the fold or cusp), like the codimension-four butterfly bifurcation found above.

The classification of such bifurcations is known to extend to vector fields of any dimension, for example in [3] they are referred to as class A_μ, singularities involving "one zero eigenvalue and a $(\mu - 1)$-fold degeneracy in the nonlinear terms", which are topologically equivalent to "principal families" of the form $\dot{x} = \pm x^{\mu+1} + P_\mu(x, \epsilon)$ where P_μ is an order $\mu - 1$ monomial in x. This, however, does not provide a practical means to locate such bifurcations in a general n-dimensional system.

To address this problem, a set of conditions have been derived which are reported in a separate paper [20]. To our knowledge these conditions have not been given previously. We give a brief account of them here, having applied them in the present paper to produce the bifurcation curves in Hetesolution, 5, 6, 7, 12.

The problem is to obtain a set of conditions to locate local bifurcation points of a system of the form

$$\dot{\mathbf{x}} = \mathbf{F}(\mathbf{x}; \boldsymbol{\mu}),$$

with variables $\mathbf{x} \in \mathbb{R}^n$ and parameters $\boldsymbol{\mu} \in \mathbb{R}^m$. In our particular system of interest $n = 4$, with $\boldsymbol{x} = (X, Z, Y, W)$, where $\boldsymbol{F}$ is the right-hand side of (3.16), and $\boldsymbol{\mu}$ is a vector consisting of some m of the independent parameters (k, r, s, a, b). Our interest is limited in scope to locating bifurcations where several zeros of $\boldsymbol{F}$ coincide, often known as *catastrophes* in dynamical systems. The method described below does not identify bifurcations involving multiple vanishing eigenvalues, or detect stability changes associated with pure imaginary eigenvalues.

We propose that the following conditions define an elementary catastrophe

underlying a bifurcation, or simply (from [20]), an *underlying catastrophe*:

$$0 = \boldsymbol{F}, \qquad [\text{equilibrium}, m = 0] \tag{3.35a}$$
$$0 = \boldsymbol{F} = \mathcal{B}_1 \neq \{\mathcal{G}_1\}, \qquad [\text{fold}, m = 1], \tag{3.35b}$$
$$0 = \boldsymbol{F} = \mathcal{B}_1 = \mathcal{B}_2 \neq \{\mathcal{G}_2\}, \qquad [\text{cusp}, m = 2], \tag{3.35c}$$
$$0 = \boldsymbol{F} = \mathcal{B}_1 = \mathcal{B}_2 = \mathcal{B}_3 \neq \{\mathcal{G}_3\}, \qquad [\text{swallowtail}, m = 3], \tag{3.35d}$$
$$0 = \boldsymbol{F} = \mathcal{B}_1 = \mathcal{B}_2 = \mathcal{B}_3 = \mathcal{B}_4 \neq \{\mathcal{G}_4\}, \qquad [\text{butterfly}, m = 4], \tag{3.35e}$$

and so on for bifurcations of higher codimension $m > 4$. The functions $\mathcal{B}_1$,...,$\mathcal{B}_m$ and $\{\mathcal{G}_m\}$ are given below. The functions $\mathcal{B}_j$ are a generalization of the derivatives that identify such catastrophes in one dimension, while each $\{\mathcal{G}_m\}$ denotes a set of derivatives used to establish non-degeneracy. These various functions are defined as follows in the case $n = 4$ that applies to (3.16); for the general expressions and further explanation see [20].

Let $\boldsymbol{x} = (X, Z, Y, W)$ and $\boldsymbol{F} = (F_1, F_2, F_3, F_4)$. A catastrophe occurs where the gradient vectors at a point $\frac{\partial F_1}{\partial \mathbf{x}}, \frac{\partial F_2}{\partial \mathbf{x}}, \frac{\partial F_3}{\partial \mathbf{x}}, \frac{\partial F_4}{\partial \mathbf{x}}$, are linearly dependent. Assuming generically that any three of these gradient vectors *are* linearly independent, then we can define the functions $\mathcal{B}_j$ as

$$\begin{aligned} \mathcal{B}_1 &= \det \left| \frac{\partial(F_1, F_2, F_3, F_4)}{\partial(X, Z, Y, W)} \right| \qquad \text{and} \\ \mathcal{B}_j &= \det \left| \frac{\partial(\mathcal{B}_{j-1}, F_2, F_3, F_4)}{\partial(X, Z, Y, W)} \right| , \end{aligned} \tag{3.36}$$

for $j > 1$. Solving $0 = \mathbf{F} = \mathcal{B}_1 = ... = \mathcal{B}_m$ then allows one to locate a catastrophe of codimension r in the space of (X, Z, Y, W) and some m parameters $(\mu_1, ..., \mu_m)$.

The non-degeneracy conditions $\{\mathcal{G}_m\}$ that ensure this system of equations is solvable are more complicated, but essential. In Thom's general theory deriving from [36], the number of conditions needed to define a given catastrophe grows faster-than-factorially with the codimension m, and is not typically solvable to find *where* any given catastrophe might occur. Under the conditions $\{\mathcal{G}_m\} \neq 0$ these reduce to a solvable system of just the r conditions $0 = \mathcal{B}_1 = ... = \mathcal{B}_m$. The non-degeneracy conditions consist of a set of functions $\{\mathcal{G}_m\} = \{\mathcal{G}_m^{k_1 ... k_{m-1}}\}$ taken over all $k_j = 1, ..., 4$, for $j = 1, ..., m-1$, (hence there are 4^{m-1} of them), which themselves are simply determinants,

$$\mathcal{G}_m^{k_1 ... k_{m-1}} = \det \left| \frac{\partial(F_1, F_2, F_3, F_4, \mathcal{B}_1, \mathcal{B}_2^{k_1} ..., \mathcal{B}_{m-1}^{k_1 ... k_{m-2}})}{\partial(X, Z, Y, W, \mu_1, ..., \mu_m)} \right| , \tag{3.37}$$

and one need only evaluate these to check they are non-zero.

The $\mathcal{B}_j^{k_1 ... k_{j-1}}$ are more general forms of each $\mathcal{B}_j$. Observe that when defining $\mathcal{B}_j$ in bifs, we have chosen to replace the first component of $\mathbf{F}$ with $\mathcal{B}_{j-1}$, but we could have chosen to replace the second, third, or fourth component of $\mathbf{F}$ instead. The functions $\mathcal{B}_j^{k_1 ... k_{j-1}}$ are all of the alternative definitions of the $\mathcal{B}_j$.

To express these let $\mathbf{F}\backslash^k Q$ denote $\mathbf{F}$ with its k^{th} component replaced by the scalar Q, so

$$F_1\backslash Q = (Q, F_2, F_3, F_4)\ , \quad F_2\backslash Q = (F_1, Q, F_3, F_4)\ ,$$
$$F_3\backslash Q = (F_1, F_2, Q, F_4)\ , \quad F_4\backslash Q = (F_1, F_2, F_3, Q)\ . \tag{3.38}$$

Then we define a sequence of Jacobian determinants $\mathcal{B}_j^{k_1\ldots k_{j-1}}$ in which we replace the k_{j-1}^{th} component of $\boldsymbol{F}$ by the previous function $\mathcal{B}_{j-1}^{k_1\ldots k_{j-2}}$, and the superscript $k_1...k_j$ keeps track of these k's,

$$\mathcal{B}_j^{k_1\ldots k_{j-1}} = \det\left|\frac{\partial(\mathbf{F}\backslash^{k_{j-1}}\mathcal{B}_{j-1}^{k_1\ldots k_{j-2}})}{\partial(X,Z,Y,W)}\right|\ , \tag{3.39}$$

for $j = 1, ..., m$, and $k_i = 1, 2, 3, 4$. Note $j = 1$ just gives the function $\mathcal{B}_1$, and bifs means we define $\mathcal{B}_j := \mathcal{B}_j^{1\ldots 1}$.

A more complete derivation of the above conditions is given in [20], with example calculations, along with more explicit forms of these $\mathcal{B}$ and $\mathcal{G}$ functions for low codimension cases, and with the geometrical explanation of where these conditions come from.

Using the above conditions, we obtain the same set of fold, cusp, and butterfly catastrophe conditions as found in sec:bif. Moreover, we can show that the bifurcations are non-degenerate; that is, the appropriate $\mathcal{G}_r$ conditions defined above are non-vanishing. The butterfly bifurcation is found to only occur when $S = E$. One obtains implicit equations for folds and cusps for $S \neq E$; we omit the full, rather lengthy, equations here. One also finds that the highest codimension bifurcation that occurs in the system is a codimension-6 star catastrophe, in which seven equilibria coincide. This occurs when $a = -\frac{1}{2}k^2$, $b = \frac{13}{108}k^3$, $r = -\frac{5}{12}k^2$, but since r is negative this is not relevant to the biological application.

3.5 Computation of steady-state solutions

The final matter to explain in Hetesolution is how we compute the coloured curves, which represent heteroclinic orbits. We have used a several-stage process. First, we use direct numerical integration of (2.2), in appropriate regions of parameter and initial condition space, to converge to a wave-pinned solution (see overalldynamic). Such steady states correspond to heteroclinic orbits in space. We can then transform such solutions into the (u, E, v, S) coordinates using formula (2.9). Finally, we continue these heteroclinic solutions as parameters vary, using the continuation software AUTO [14]. Specifically, we implement asymptotic boundary conditions which demand that the boundary points should lie in the appropriate stable or unstable eigenspace of the linearisation at each of the two distinct equilibria. This is based on the method implemented by HomCont within AUTO, see in particular the demo `she` [14].

tracs shows in more detail how the heteroclinic solutions relate to these different equilibria and their bifurcations. On the symmetry line $S = E$, a

heteroclinic solution connects the equilibria we labelled $(X_1^{\pm}, Y_1^{\pm})$, shown for a typical parameter value by (a). At (b) a global bifurcation occurs in which this heteroclinic solution connects $(X_1^{\pm}, Y_1^{\pm})$ both to (X_I, Y_I). At this point this curve of heteroclinic solutions intersects two other curves, on which we take the points (e) and (f) as typical examples, on which lie heteroclinic solutions connecting (X_I, Y_I) to either (X_1^+, Y_1^+) (as at (f)) or (X_1^-, Y_1^-) (as at (e)). These curves of heteroclinic solutions terminate at fold curves at (c) and (d), at which the heteroclinic orbit connects (X_1^+, Y_1^+) to (X_I, Y_I) as it undergoes a fold with (X_2^-, Y_2^-) (at (c)), or the heteroclinic orbit connects (X_1^-, Y_1^-) to (X_I, Y_I) as it undergoes a fold with (X_2^+, Y_2^+) (at (c)).

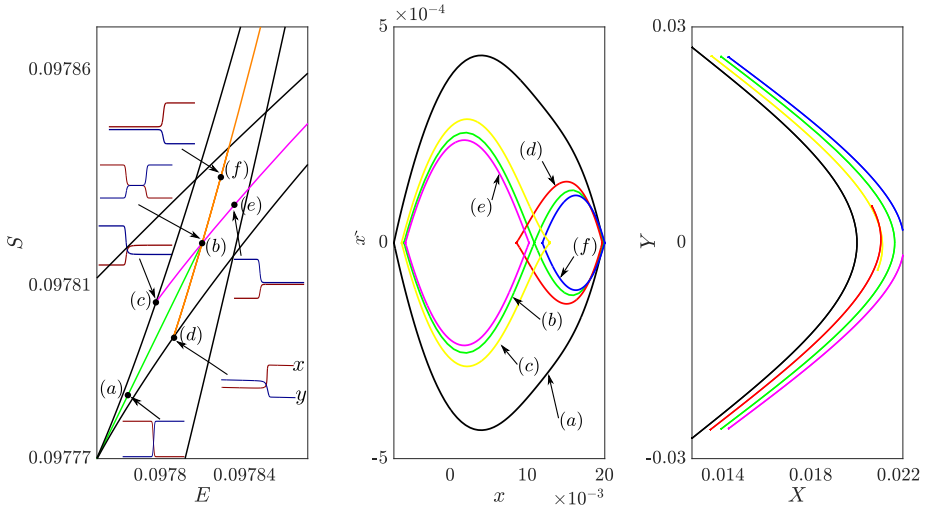

Figure 5: Left panel: bifurcation diagram for (3.12) with $\eta = 2$, $\mu = 0.05$, $\rho = 0.06$, $\alpha = 0.005$ and $\delta = 0.10995$. Graphs of heteroclinic orbits are shown inset, for the profiles a-e) from Hetesolution. The middle and right panels show the same orbits in the state space of (x, x') and (X, Y).

All of the dynamics we have computed is found to be destroyed in a butterfly catastrophe, as we shall explain in the next section. In fact there are two butterflies. In this situation the butterfly catastrophe can be considered to be of codimension three; that is, it would occur along a curve in the four-dimension (E, S, η, δ)-space. Each butterfly destroys pairs of symmetric cusps in this system and the corresponding heteroclinic connections between the equilibria involved. Note that the butterfly bifurcation which according to our classification above would ordinarily be of codimension four, is effectively of codimension three in this system if the cusps occur along the line $E = S$. There are thus two butterfly catastrophes, destroying each of the two pairs of cusps (see NumericalAbley2 below). The values of δ against η for which butterfly catastrophes occur are plotted in butterfly.

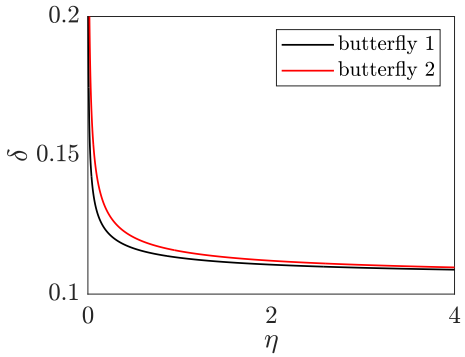

Figure 6: The bifurcation diagram for both curves of butterfly catastrophes in the (η, δ)-plane. The remaining parameter values are as in Hetesolution.

4 Transitions of homogeneous and heteroclinic solutions

We now discuss what happens under variation of the system parameters. As a primary bifurcation parameter we choose the diffusion ratio δ. We seek to understand the transition of the number of steady-state solutions, from the diagram in Hetesolution, to the situation that occurs in the upper portion of butterfly beyond both butterfly catastrophe curves, in which there is a single steady state and no longer any heteroclinic connections. NumericalAbley2 shows a series of snapshots of the steady-state and the heteroclinic bifurcation diagram in (E, S)-plane, for increasing set values of δ, for fixed η. All computations have been carried out in AUTO. We find that a similar sequence of transition can be found to occur for any value of $\eta \to 0$ as we increase δ towards and beyond the red curve on which the butterfly catastrophe occurs in the (η, δ)-plane in butterfly.

We shall start from NumericalAbley2(a), which is identical to Hetesolution. For these parameter values, we have nine separate homogeneous steady-state solutions. Also, there are five different kinds of heteroclinic solutions, which lie on the different coloured curves in the diagram. Profiles of each kind of solution was given in Hetesolution. Also notice the two special points that are labelled with an asterisk. Here is where a codimension-two heteroclinic cycle exists between a pair of steady states, resulting in 'front and back' type solutions.

Increasing δ from 0.08 beyond 0.1 results in a change of topology of the fold and cusp curves, leading to there being a maximum of five steady states (see NumericalAbley2(b)–(d)). Through these changes though, the number of heteroclinic solutions that occur does not change.

Further increasing the δ value destroys two heteroclinic solution branches through the first butterfly catastrophe (see NumericalAbley2(d) and (e)), as explained in comut. NumericalAbley2(f) shows the situation after the second butterfly catastrophe takes place; it is clear that two further heteroclinic branches

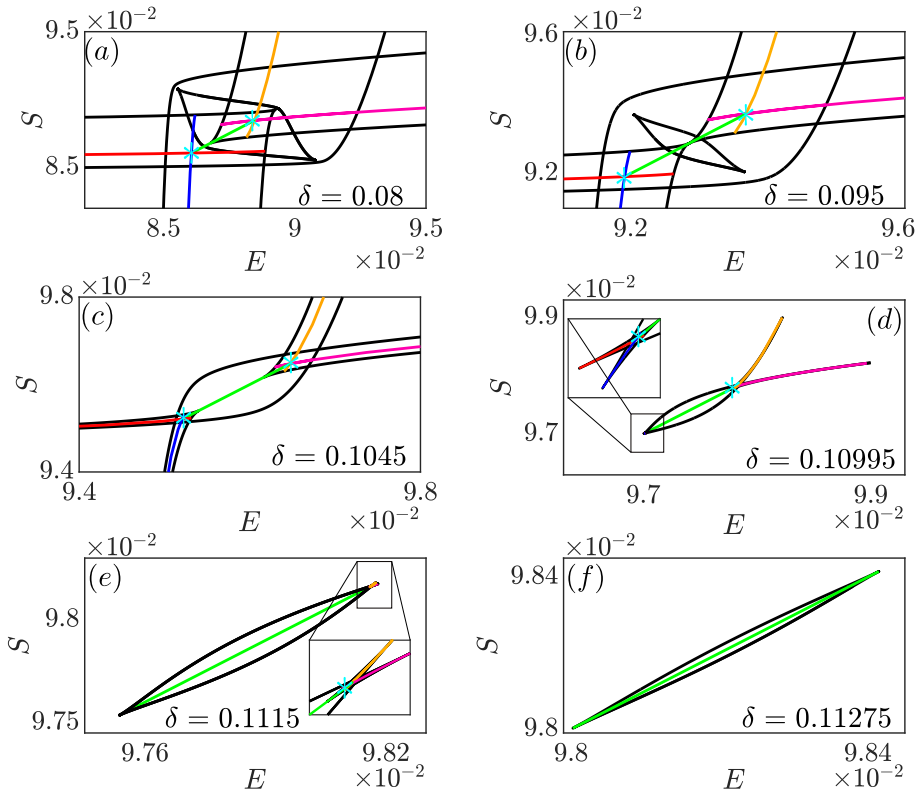

Figure 7: Bifurcation diagram of (3.11) showing the transition of homogeneous steady states as we vary the three parameter E, S and δ, with fixed $\eta = 2$, $\mu = 0.05$, $\rho = 0.06$, $\alpha = 0.005$.

have been destroyed.

Finally, we are left with a thin region bounded by a pair of fold curves that meet at cusps and contain a single heteroclinic connection NumericalAbley2(f). We find that for $\delta \approx 0.1122$ these two cusps annihilate each-other and there are no heteroclinic solutions at all for higher δ-values.

5 Polarity formation: solution to the initial-value problem

Note that E and S are not invariants of the PDE system, instead they can be consider as constants that parameterise different families of steady-state solutions. However, for a given domain size 2ℓ, each different value of E and S along a family of heteroclinic or homogeneous solutions will typically have different value of A_T and B_T, which are invariants of the full time-dependent PDEs. On

such a finite domain, translation of a heteroclinic solution in space will typically lead to different values of A_T and B_T. Thus we can ask the question for a given value of A_T and B_T, is there a unique steady state that the solution evolves to, or is the final obtained state a sensitive function of the initial data? This solution would then represent the wave-pinned final state of the system for the given initial values of A_T and B_T.

All results presented here are for the fixed domain size $\ell = 100$ and for the same parameter values as in Hetesolution. We have also performed simulations with both smaller and larger domain sizes. In each case the results are found to be qualitatively the same as presented below in polaryFig, but the overall values of A_T and B_T vary with domain size. Remarkably, we have found no evidence of multi-stability. That is, for each choice of values of A_T and B_T, for a given set of system parameters there appears to be a unique final steady state that is reached by the initial-value problem, irrespective of what initial data we take.

We simulate the full PDE system (2.2) at a fixed set of η, μ, ρ, α and δ. All simulations were carried out in Matlab. For all initial conditions, we find that the dynamics always settles to steady state. Note that the S and E values of the final steady state are emergent properties that are found to be always a unique function of the values of A_T and B_T, for every initial run we tried. atbt summarises the results for the same parameter values in Hetesolution. In each coloured region we run multiple simulation from pseudo random initial conditions containing Heaviside-style jumps. In each case the simulations revealed qualitatively the same behaviour in each coloured region. We obtain the boundaries between the coloured regions by choosing the values of E and S to lie on the appropriate coloured curves in Hetesolution to represent the particular heteroclinic connection in (2.6). Then we shift the solution phase, that is the location in x of the heteroclinic jump, from the rightmost ($x = \ell$) to the leftmost ($x = -\ell$) point in the domain.

The simulation results for the parameter set in Hetesolution reveal eight distinct regions, see polaryFig. The white regions represent the un-polarised area in which homogeneous steady states are obtained (see the solution profile (h)). The yellow and cyan regions are associated with the heteroclinic connection that has large differences between the polarised and depolarised A^*, and more negligible differences between the polarised and depolarised B^*. The two regions differ in their overall concentration of B^*. In the yellow region, B^* is always in large excess of inactive B and close to the polarised amount of A^*. Whereas in the cyan region, the overall concentration of B^* is much lower and commensurate with the depolarised amount of A^* (see the solution profiles (a) and (c) in atbt). In contrast, the green and the orange regions show heteroclinic orbits that have a larger difference between the polarised and depolarised B^*, and smaller difference between the polarised and depolarised A^*. In the green region, the value of A^* is nearby the polarised amount of the B^* and far from the inactive A. In contrast, in the orange region A^* is closer to the depolarised amount of B^* (see the solution profiles (b) and (d) in atbt). The pink region corresponds to an intermediate polarity solution where A^* and B^* have the same

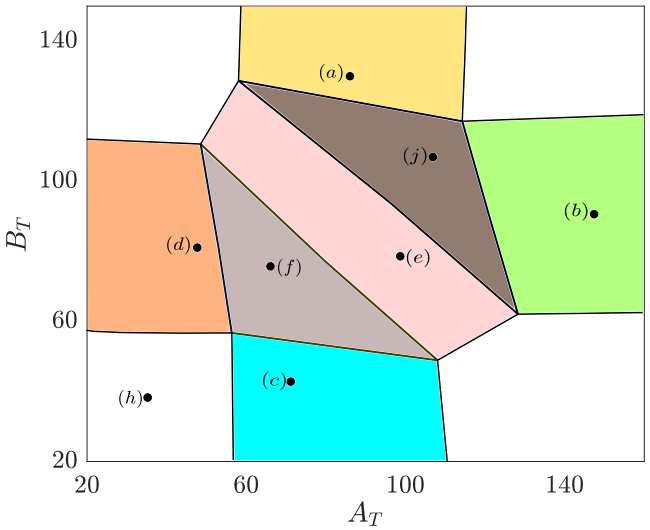

Figure 8: Summary in the (A_T, B_T)-space of initial conditions of the different form of steady state solutions reached via solution of the initial value problem for the model (2.6), with parameter values as in Hetesolution and domain length $\ell = 100$. Here, white regions correspond to where homogeneous steady states are reached, and each different color shading represents a different qualitative type of wave-pinned state. To illustrate the different forms of wave-pinning, labeled points (a)–(h) indicate the parameter of the corresponding panel in atbt in which the solution profile is given. Zooms showing the morphology of the solution profiles within the cyan and brown regions are given in zoomcyan and zoomGregion.

height but different directions (see the solution profile (e) in atbt). Finally, the brown and the grey regions are related to a particular polarity state that joins the dominant polarity state to the intermediate state. The difference between the two regions is that, for the solution in the brown region, the intermediate state has high concentration, whereas in the grey region the intermediate state has low concentration (see the solution profiles (f) and (j) in atbt).

In zoomcyan, we zoom in on the cyan region in polaryFig to show that there is a distinct polarised solution, with different phase shifts representing different values of E and S along the red curve labelled C in Hetesolution. Specifically, the profiles (a), (b) and (c) shown in zoomcyan represent solutions for varying values of E and S along the red curve in Hetesolution, while the profiles (b), (d), and (e) exhibit solutions for the similar values of E and S but with various phase shifts. In zoomGregion we zoom in on the brown region of polaryFig, to demonstrate that the behaviours we obtain in zoomcyan are representative of all the regions presented in polaryFig. The solutions in the brown region have the same value of E and S represented by an asterisk in Figure 1. Now, to

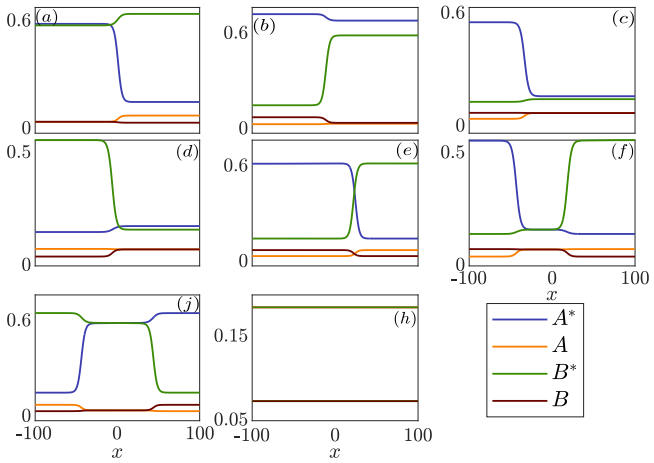

Figure 9: Example of the stable polarized steady state from each different region in polaryFig.

shift to a different solution within this region, we can vary two distinct phase shifts representing the two heteroclinic connections making up the profile at this special point in the (E, S)-plane.

6 Other Models

So far we have only considered results for model II. We have performed the same analysis for each of models I-IV, whose kinetic functional forms were given in (2.5)-(2.8). The analysis in each case is similar, and we shall omit most of the details for simplicity. In some cases, the bifurcation diagrams are considerably simpler, owing to there being fewer possible homogeneous equilibria. Thus, the analysis we have so far found is representative of the most complex results that we have so far found in systems of this type. We restrict our result in this section just to presentation of the analogous final results for models I,III and IV.

ableyexhibits the bifurcation diagram for Model I, with kinetics (2.6). The black curve shows the pairwise annihilation among the steady states, and the green curve denotes the symmetric line of the system with $E = S$. This system has only one type of heteroclinic solution which is on the symmetry line where $E = S$. This is the intermediate polarised state as in atbt E. Furthermore, this heteroclinic solution is destroyed at a single cusp bifurcation.

RacRoH displays the bifurcation diagram for Model IV, which captures mutual inhibition (2.8). In general, the bifurcation diagram is similar to Model II, except that there is a rather simpler termination of heteroclinic solutions at two cusp bifurcations.

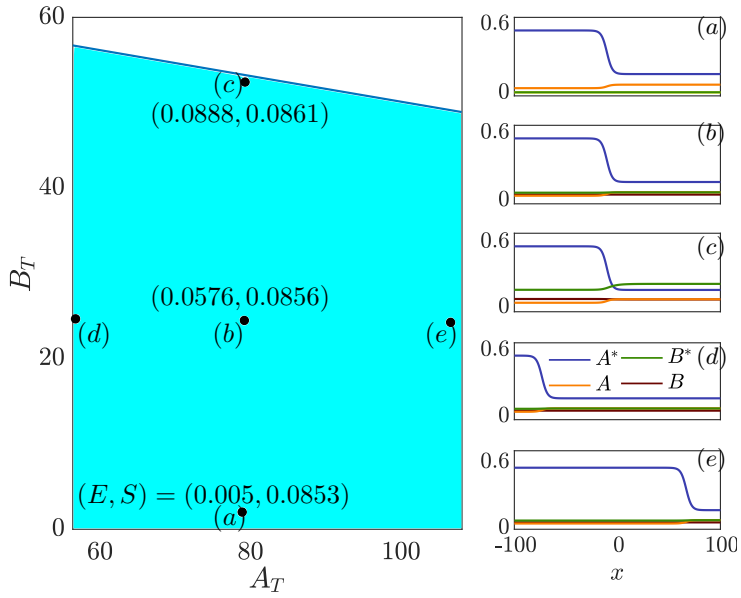

Figure 10: Zoom in the cyan region in polaryFig, showing the morphology of the wave-pinned steady state within the region.

jucy expresses the bifurcation diagram for model III, (2.7). The bifurcation diagram is qualitatively analogous to Hetesolution.

To conclude this section, we provide another numerical example to support the observations that for each value of E and S in $S_E bifurcation, thereisadistinctpolarisedsolutionwithdifferen$ 1001[18].

7 Conclusion

This paper has provided a framework for understanding how asymmetric morphologies arise within simple four-species activator-inhibitor models of the form (2.2), representing the inactive and active forms of two G-proteins. We give some answers to why certain heteroclinic connections exist in certain parts of parameters space. The key property of the model that makes this analysis possible is that the overall concentration of each protein-type ($A + A^*$ and $B + B^*$) is conserved. This conservation principle leads to two special properties of the dynamics. First, the steady-state system is degenerate, and can be written in the form (2.10) in which E and S are first integrals that, owing to the Neumann boundary conditions, are constant in space for steady-state solutions. Second, for the initial-value problem, the initial amounts of A-species and B-species parameterise which steady state or heteroclinic connection the dynamics relaxes to, and where, within a fixed computational domain, the sharp "wave-pinned" transition should settle. The results we have obtained confirm the experimental

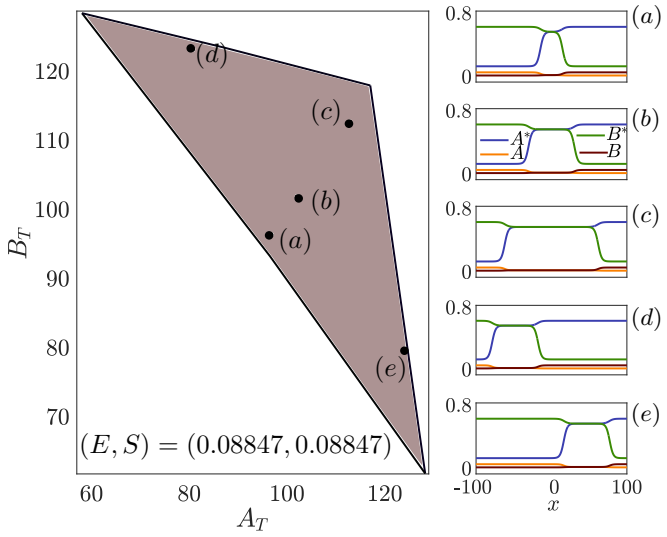

Figure 11: Zoom in the brown region in polaryFig, showing the morphology of the wave-pinned steady state within the region .

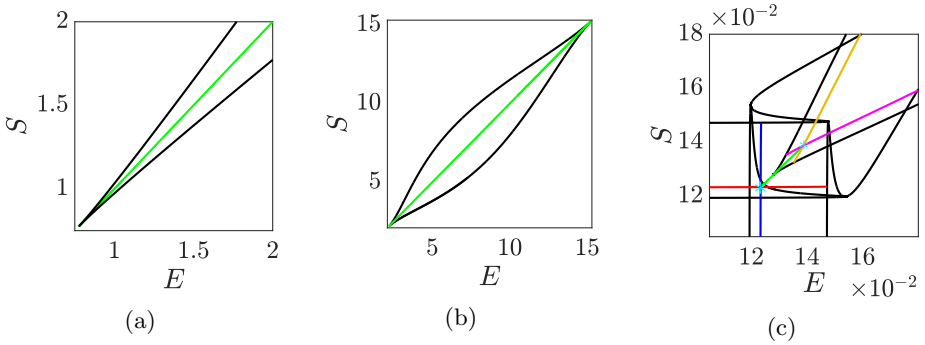

Figure 12: Bifurcation diagram in the (E, S)-plane of the models (2.5) , (2.8) and (2.7), respectively. (a) Parameter values: $\alpha = 0.005$, $\delta = 0.03$, $\eta = 0.119$, $\mu = 0.05$ and $\rho = 0.06$. (b) Parameter values: $\alpha = 0.66$, $b = 0.1$, $d = 1$ and $\delta = 0.5$. (c) Parameter values: $\alpha = 80$, $\beta = 0.12$, $c_a = 20$, $\delta = 0.08$, $\eta = 1$, $\mu = 0.5$ and $\rho = 0.2$.

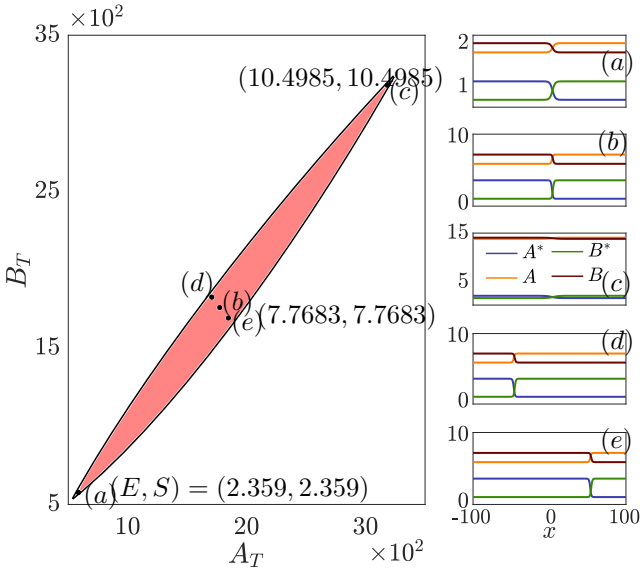

Figure 13: The equivalent of polaryFig and atbt but for the system (2.8) which has simpler behavior. Parameter values $\alpha = 0.66$, $b = 0.1$, $d = 1$ and $\delta = 0.5$, with domain length $\ell = 100$.

results in [1, 16] and some of the numerical observations in [18, 19, 25, 45].

An interesting feature of the results is that the nature of the nonlinearity does not seem particularly crucial. Most of the results have been presented for what we call Model II, an adaptation to that derived by Abley *et al.* [1]. Nevertheless we have shown in Sec. 6 how different kinetic terms considered in the literature lead to similar results, albeit with some models having less multiplicity of homogeneous and steady-state patterns within the regions of parameter space considered. Another interesting feature is that much of the behaviour found is dependent on there being a small diffusion ration between the activator and inhibitor species, a relation that might make a mathematical biologist think of Turing instability, but which is not observed in these species-conserving models (although, see the discussion in [11] for connections between different forms of pattern-formation instability mechanisms when viewed within a larger parameter space).

It should be stressed that the analysis in this paper represents only a first step to understand how wave-pinning theory may explain polarity formation observed in biology Buttenschön *et al* have recently considered several extensions of the simple 1D models of the form (1.1) or (2.2) to include mechanical feedback from the active G-proteins dynamics to cell shape and motion, see [7, 8]. There they explain how the fronts of active G-proteins allow for differential growth, leading to polarity formation that can account for the motion of animal cells. Inspired instead by the case of plant cells, an extension to models of the form (1.1) was

considered in [39, 40], where small source and loss terms were added to both the active and inactive forms. Such perturbations break the conservation law and, in an appropriate region of parameter space, lead to localised patterns rather than fronts (homoclinic rather than heteroclinic orbits). Lui *et al* [23] showed that this model on a 2D domain is capable of reproducing spot-like patterns, a conclusion which is echoed by Breña-Medina *et al.* [6]. for a model of auxin-mediated G-protein dynamics in root-hair cells.

Future work [2] shall consider what happens to the patterns formed by models of the form (1.1) with two or more ROP species, under the addition of small source and loss terms. The key mathematical question is to try to understand, as was the case in [39], how open parameter regions of heteroclinic front-like motions transform into homoclinic connections. This may shed light on how, in the context of plant biology, localised lobes and indentations may form in the so-called jigsaw-instability of leaf pavement cells [9].

Other ongoing work will consider more realistic models of G-protein dynamics where active components are bound to the cell membrane, which naturally leads to bulk-surface partial differential systems as in [24, 29]. There are many further aspects to cell polarity for which mathematical models can shed light, notably the downstream implications of the G-protein pattern. For example, the work of Dawes and collaborators, e.g. [35, 41] considers mathematical models for the effects of G-protein patterns on patterns of PAR proteins and on microtubule networks, which are thought to be responsible for delivering the proteins necessary for differential growth.

A key role here has been played by a novel application of classical catastrophe theory to vector fields. The details of that theory will appear elsewhere [20]. This has enabled us to classify and explain the different bifurcations in homogeneous steady-states and their heteroclinic connections that can occur for spatial dynamical systems of the form (2.10), in which either system parameters or first integrals S and E are varied. There are likely other problems in pattern formation theory in the presence of conserved quantities that may benefit from this approach. See for example the work of Holl *et al.* [17] on models for phase-field crystals.

References

[1] K. Abley, P. B. D. Reuille, D. Strutt, A. Bangham, P. Prusinkiewicz, A. F. M. Marée, V. A. Grieneisen, and E. Coen. An intracellular partitioning-based framework for tissue cell polarity in plants and animals. Development, 140(10):2061–2074, 2013.

[2] F. Al Saadi, A. Champneys, M. Jeffrey, V. Grieneisen, and A. Marée. Interdigitation patterns in cell polarity models without mass conservation, 2022. In preparation.

[3] V. I. Arnold, V. Afrajmovich, Y. S. Il'yashenko, and L. Shil'nikov. Dynamical systems V: bifurcation theory and catastrophe theory, volume 5. Springer Science & Business Media, 2013.

[4] A. Berken, C. Thomas, and A. Wittinghofer. A new family of RhoGEFs activates the Rop molecular switch in plants. Nature, 436(7054):1176—1180, 2005.

[5] J. J. Blakeslee, A. Bandyopadhyay, O. R. Lee, J. Mravec, B. Titapiwatanakun, M. Sauer, S. N. Makam, Y. Cheng, R. Bouchard, J. Adamec, M. Geisler, A. Nagashima, T. Sakai, E. Martinoia, J. Friml, W. A. Peer, and A. S. Murphy. Interactions among pin-formed and p-glycoprotein auxin transporters in arabidopsis. The Plant Cell, 19(1):131–147, 2007.

[6] V. Breña–Medina, D. Avitabile, A. Champneys, and M. Ward. Stripe to spot transition in a plant root hair initiation model. SIAM Journal on Applied Mathematics, 75:1090–1119, 2015.

[7] A. Buttenschön, L. Y., and E.-K. L. Cell size, mechanical tension, and GTPase signaling in the single cell. Bulletin of Mathematical Biology, 82:32016583, 2020.

[8] A. Buttenschön, L. Y., and E.-K. L. Spatio-temporal perturbations as a mechanism of cell repolarization, 2022. Preprint, University of British Columbia.

[9] R. Carter, Y. Sánchez-Corrales, M. Hartley, V. Grieneisen, and A. Marée. Pavement cells and the topology puzzle. Development, 144:4386–4397, 2017.

[10] R. Carter, Y. E. Sánchez-Corrales, M. Hartley, V. Grieneisen, and A. F. M. Marée. Pavement cells and the topology puzzle. Development, 144:4386–4397, 2017.

[11] A. Champneys, F. Al Saadi, V. Breña–Medina, V. Grieneisen, A. Marée, N. Verschueren, and B. Wuyts. Bistability, wave pinning and localisation in natural reaction-diffusion systems. Physica D., 416:art. no. 132735, 2021.

[12] L. Deshu, R. Huibo, and F. Ying. Rop GTPase-mediated auxin signaling regulates pavement cell interdigitation in arabidopsis thaliana. Journal of Integrative Plant Biology, 57(1):31–39, 2015.

[13] J. Dettmer and J. Friml. Cell polarity in plants: When two do the same, it is not the same.... Current Opinion in Cell Biology., 23:686–696, 2011.

[14] E. Doedel and B. Oldeman. Auto 07p: Continuation and bifurcation software for ordinary differential equations, 2019. github.com/auto-07p/auto-07p.

[15] L. Edelstein-Keshet, W. Holmes, M. Zajac, and M. Dutot. From simple to detailed models for cell polarization. Philosophical Transactions of the Royal Society of London B: Biological Sciences, 368, 2013.

[16] V. Grieneisen, A. Marée, and L. Østergaard. Juicy stories on female reproductive tissue development: Coordinating the hormone flows. Journal of Integrative Plant Biology, 55(9):847–863, 2013.

[17] M. Holl, A. Archer, and U. Thiele. Efficient calculation of phase coexistence and phase diagrams: application to a binary phase-field crystal model. J. Phys. Condens. Matter, 33:115401, 2021b.

[18] W. Holmes and L. Edelstein-Keshet. Analysis of a minimal rho-GTPase circuit regulating cell shape. Physical Biology, 13(4):046001, 2016.

[19] W. R. Holmes. An efficient, nonlinear stability analysis for detecting pattern formation in reaction diffusion systems. Bulletin of Mathematical Biology, 76(1):157–183, 2014.

[20] M. Jeffrey. Catastrophe conditions for vector fields and varieties in $\mathbb{R}^n$. J. Phys. A., 55:464006:1–25, 2022.

[21] J. Kleine-Vehn and J. Friml. Polar targeting and endocytic recycling in auxin-dependent plant development. Annual Review of Cell and Developmental Biology, 24(1):447–473, 2008.

[22] O. Leyser. Auxin, self-organisation, and the colonial nature of plants. Current Biology, 21(9):R331 – R337, 2011.

[23] R. E. Lui, Y. and E.-K. L. Spots, stripes, and spiral waves in models for static and motile cells : GTPase patterns in cells. Journal of Mathematical Biology, 82:33660145, 2021.

[24] A. Madzvamuse, A. Chung, and C. Venkataraman. Stability analysis and simulations of coupled bulk-surface reaction-diffusion systems. Proc. Roy. Soc. Lond. A, 471:20140546, 2015.

[25] Y. Mori, A. Jilkine, and L. Edelstein-Keshet. Wave-pinning and cell polarity from a bistable reaction-diffusion system. Biophysical journal, 94(9):3684–3697, 2008.

[26] Y. Mori, A. Jilkine, and L. Edelstein-Keshet. Asymptotic and bifurcation analysis of wave-pinning in a reaction-diffusion model for cell polarisation. SIAM J. Appl. Math., 71:1401–1427, 2011.

[27] S. Nagawa, T. Xu, and Z. Yang. RHO GTPase in plants. Small GTPases, 1(2):78–88, 2010.

[28] X. Pan, J. Chen, and Z. Yang. Auxin regulation of cell polarity in plants. Current Opinion in Plant Biology, 28:144 – 153, 2015.

[29] F. Paquin-Lefebvre, W. Nagata, and M. Ward. Pattern formation and oscillatory dynamics in a two-dimensional coupled bulk-surface reaction-diffusion system. SIAM J. Appl. Dyn. Sys., 18:1334–1390, 2019.

[30] T. Poston and I. Stewart. Catastrophe Theory and Its Applicaitons. Dover, New York, 1997.

[31] M. Raftopoulou and A. Hall. Cell migration: Rho GTPases lead the way. Developmental Biology, 265(1):23 – 32, 2004.

[32] D. Reinhardt, T. Mandel, and C. Kuhlemeier. Auxin regulates the initiation and radial position of plant lateral organs. The Plant Cell, 12(4):507–518, 2000.

[33] T. Sachs. Cell polarity and tissue patterning in plants. Development, 112(SUPPL. 1):83–93, 1991.

[34] Y. Sánchez-Corrales, M. Hartley, J. van Rooij, A. Marée, and V. A. Grieneisen. Morphometrics of complex cell shapes: lobe contribution elliptic Fourier analysis (LOCO-EFA). Development, 145:dev156778, 2018.

[35] S. Seirin-Lee, E. Gaffney, and A. Dawes. CDC-42 Interactions with PAR proteins are critical for proper patterning in polarization. cells. Cells, 9:2036, 2020.

[36] R. Thom. Les singularités des applications différentiables. Ann. Inst. Fourier, 6:43–87, 1955-6.

[37] K. Urszula, M. Fendrych, and J. Friml. Polar delivery in plants; commonalities and differences to animal epithelial cells. Open Biology, 4:140017, 2014.

[38] K. van Berkel, R. J. de Boer, B. Scheres, and K. ten Tusscher. Polar auxin transport: models and mechanisms. Development, 140(11):2253–2268, 2013.

[39] N. Verschueren and A. Champneys. A model for cell polarization without mass conservation. SIAM Journal on Applied Dynamical Systems, 16:1797–1830, 2017.

[40] N. Verschueren and A. Champneys. Erratum: A model for cell polarization without mass conservation. SIAM Journal on Applied Dynamical Systems, 18:594–595, 2019.

[41] D. White, G. de Vries, J. Martin, and A. Dawes. Microtubule patterning in the presence of moving motor proteins. J. Theor. Biol., 382:81–90, 2015.

[42] T. Xu, M. Wen, S. Nagawa, Y. Fu, J.-G. Chen, M.-J. Wu, C. Perrot-Rechenmann, J. Friml, A. M. Jones, and Z. Yang. Cell surface- and Rho GTPase-based auxin signaling controls cellular interdigitation in arabidopsis. Cell, 143(1):99 – 110, 2010.

[43] Z. Yang. Small GTPases. The Plant Cell, 14(suppl 1):S375–S388, 2002.

[44] Z. Yang. Cell polarity signaling in arabidopsis. Annual Review of Cell and Developmental Biology, 24(1):551–575, 2008.

[45] C. Zmurchok and W. Holmes. Simple Rho GTPase dynamics generate a complex regulatory landscape associated with cell shape. Biophysical Journal, 118(6):1438–1454, 2020.